



CHORUS

This is the accepted manuscript made available via CHORUS. The article has been published as:

Plasmon mode as a detection of the chiral anomaly in Weyl semimetals

Jianhui Zhou, Hao-Ran Chang, and Di Xiao

Phys. Rev. B **91**, 035114 — Published 13 January 2015

DOI: [10.1103/PhysRevB.91.035114](https://doi.org/10.1103/PhysRevB.91.035114)

Plasmon mode as a detection of the chiral anomaly in Weyl semimetals

Jianhui Zhou,^{1,*} Hao-Ran Chang,^{2,†} and Di Xiao¹

¹*Department of Physics, Carnegie Mellon University, Pittsburgh, Pennsylvania 15213, USA*

²*Department of Physics and Institute of Solid State Physics, Sichuan Normal University, Chengdu, Sichuan 610066, China*

Weyl semimetals are one kind of three dimensional gapless semimetals with nontrivial topology in the momentum space. The chiral anomaly in Weyl semimetals manifests as a charge imbalance between the Weyl nodes of opposite chiralities induced by parallel electric and magnetic fields. We investigate the chiral anomaly effect on the plasmon mode in both intrinsic and doped Weyl semimetals within the random phase approximation. We prove that the chiral anomaly gives rise to a new plasmon mode in intrinsic Weyl semimetals. We also find the chiral anomaly leads to some exotic properties in the plasmon dispersion in doped Weyl semimetals. Consequently, the unconventional plasmon mode acts as a signature of the chiral anomaly in Weyl semimetals, by which the spectrum of plasmon provides a proper way to detect the Lifshitz transition.

PACS numbers: 71.90.+q, 03.65.Vf, 73.43.-f, 71.45. Gm

I. INTRODUCTION

Weyl semimetals¹ (SMs) are a new class of gapless topological phase, which can be seen as three dimensional (3D) analogs of graphene. Weyl fermions emerge from the band degenerate points—the Weyl nodes—in the momentum space, which are characterized by their chirality. Due to the fermion doubling theorem², Weyl nodes with opposite chirality always appear in pairs. Each Weyl node behaves like a magnetic monopole in the momentum space, which acts as the source/drain for the Berry curvature field³. It has been predicted that this nontrivial momentum-space topology of Weyl nodes gives rise to a number of novel electromagnetic responses^{4–16}. On the material side, Weyl SMs have been proposed for strongly correlated iridates¹⁷, semiconductor heterostructures^{18,19}, and other materials^{20–23}. In addition, 3D Dirac materials have recently been realized in both Cd₃As₂^{24,25} and Na₃Bi^{26,27}, which could greatly facilitate the search for Weyl SMs.

A remarkable phenomenon associated with Weyl nodes is the so-called chiral anomaly^{28,29}, in which the application of a pair of parallel electric field \mathbf{E} and magnetic field \mathbf{B} induces a charge imbalance between the two Weyl nodes with opposite chirality. This chiral anomaly can be utilized to detect 3D Weyl SMs in experiments. For example, a large longitudinal magnetoresistivity was proposed as a consequence of the chiral anomaly², which, however, is difficult to identify unambiguously in magnetotransport data³⁰. Recently, nonlocal transport³¹, optical conductivity^{32,33}, and optical absorption³⁴ measurements have also been proposed to probe the chiral anomaly in 3D Weyl SMs.

In this paper, we propose an alternative detection method of the chiral anomaly by employing the plasmon mode in 3D Weyl SMs. We show that the chiral anomaly would lead to a new plasmon mode in intrinsic Weyl SMs. The chiral anomaly causes a redshift of the frequency of plasmon mode in doped Weyl SMs. Once the small Fermi surface crosses the Weyl node that corresponds to the

Lifshitz transition (LT) point, the frequency turns out to be a violetshift. Therefore, the plasmon mode can be regarded as a signature of the chiral anomaly in 3D Weyl SMs. We also show how to extract the information of the LT point from the plasmon dispersion.

The rest of this work is organized as follows. In Sec. II, we discuss the chiral anomaly effect in Weyl SMs and outline the formalism for plasmon. In Sec. III, we prove the existence of a new plasmon mode due to the chiral anomaly in undoped Weyl SMs and calculate the plasmon dispersion. In Sec. IV, we consider the chiral anomaly effect on the plasmon mode in doped Weyl SMs and discuss the chiral anomaly-driven Lifshitz transition. In Sec. V, we summarize the main results of this paper. Finally, in Appendices A and B we give details of the calculation of the free polarization function.

II. MODEL AND FORMALISM

We begin with a low-energy effective Hamiltonian for Weyl fermions in the vicinity of the Weyl node of chirality $\chi = \pm$:

$$\mathcal{H} = \chi \hbar v_F \mathbf{k} \cdot \boldsymbol{\sigma} - \mu_\chi, \quad (1)$$

where v_F is the Fermi velocity, $\boldsymbol{\sigma} = (\sigma_x, \sigma_y, \sigma_z)$ refers to the three Pauli matrices, and μ_χ stands for the chirality-dependent chemical potential given by a superposition of the equilibrium carrier density and the pumped carrier density originating from the chiral anomaly. The latter grows linearly with time but the large momentum internode scattering would counteract this imbalance of carriers between two Weyl nodes. Eventually the system reaches a non-equilibrium steady state characterized by an internode relaxation time τ_v that had been evaluated microscopically³¹. Consequently, the density of electrons pumped into or out of the neighborhood of Weyl node χ can be expressed as²

$$\Delta\rho_\chi \equiv \chi \frac{e^2}{4\pi^2 \hbar^2} \mathbf{E} \cdot \mathbf{B} \tau_v. \quad (2)$$

We also define several chirality-dependent quantities: the fermi wave vector $k_{F\chi}^3 = 6\pi^2 n_\chi$, the chemical potential $\mu_\chi = \hbar v_F k_{F\chi}$, and the charge density $n_\chi = n + \Delta\rho_\chi$. When the two Weyl nodes are equally populated, the corresponding Fermi wave vector and the chemical potential become $k_F^3 = 6\pi^2 n$, $\mu = \hbar v_F k_F$. For convenience, we restrict our discussion to $\mathbf{E} \cdot \mathbf{B} > 0$. For the undoped case with vanishing equilibrium chemical potential, μ_χ depends only on the pumped charge associated with the chiral anomaly:

$$\mu_\chi = \chi \left(\frac{3e^2 \hbar v_F^3}{2} \mathbf{E} \cdot \mathbf{B} \tau_v \right)^{\frac{1}{3}}. \quad (3)$$

Meanwhile for the doped case with a finite chemical potential μ , we obtain the corresponding chirality-dependent chemical potential as

$$\mu_\chi = (1 + \chi\gamma^3)^{1/3} \mu, \quad (4)$$

where we have introduced a dimensionless ratio between the pumped charge and the equilibrium charge

$$\gamma = \left(\frac{3e^2 \hbar v_F^3 \mathbf{E} \cdot \mathbf{B} \tau_v}{2\mu^3} \right)^{1/3}. \quad (5)$$

It follows from Eq. (5) that by tuning the external fields the system undergoes a chirality-dependent LT at $\gamma = \pm 1$, i.e., the change of the topology of the chirality-dependent Fermi surface. In the following we shall work in the weak magnetic field limit³⁵, thus neglect the Landau level structure of Weyl nodes³¹⁻³⁴. In addition, we will focus on the n -doped case with a finite positive equilibrium chemical potential $\mu > 0$ throughout this paper (the discussion of the p -doped case is similar).

It has been demonstrated that no plasmon exists in undoped Weyl or Dirac SMs^{36,38} within the random phase approximation (RPA). However, when the chiral anomaly occurs, the anomalous charge transfer between the two Weyl nodes forces the Fermi surfaces to move away from their equilibrium position in opposite directions as shown in Fig. 1. Thus the chemical potentials of the two Weyl nodes are μ_+ and μ_- satisfying the relation $\mu_+ = -\mu_- \equiv \mu > 0$. In principle, the metallic nature of intrinsic Weyl SMs with chiral anomaly would support plasmon modes. In the following, we present an exact and general proof of the existence of the novel plasmon due to the chiral anomaly in undoped Weyl SMs.

The general form of the wave vector q - and frequency ω -dependent dielectric function within the RPA is given by

$$\varepsilon(q, \omega) = 1 - V(q)\Pi(q, \omega), \quad (6)$$

where $V(q) = 4\pi e^2 / \kappa q^2$ is the Fourier transform of the 3D Coulomb interaction with κ being the effective dielectric constant. Let us consider one of the Weyl nodes. The noninteracting polarization function $\Pi(q, \omega)$ reads (see Appendix A)

$$\Pi(q, \omega) = \frac{g}{L^3} \sum_{\mathbf{k} s s'} \frac{f(\epsilon_{\mathbf{k}s}) - f(\epsilon_{\mathbf{k}'s'})}{\hbar\omega + \epsilon_{\mathbf{k}s} - \epsilon_{\mathbf{k}'s'} + i\eta} F_{ss'}(\mathbf{k}, \mathbf{k}'), \quad (7)$$

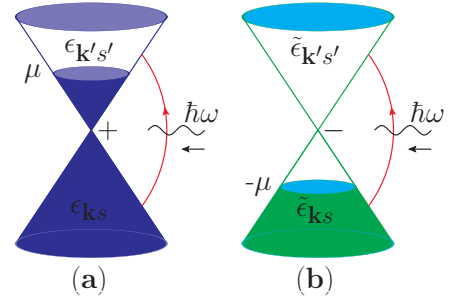


FIG. 1: (Color online) The distribution of electrons in the two Weyl nodes $\chi = \pm$ induces by the chiral anomaly ($\mathbf{E} \cdot \mathbf{B} \neq 0$) in undoped Weyl SMs.

where g is the number of pairs of Weyl nodes, η is a positive infinitesimal, and $s, s' = \pm$ are the band indices. The overlap of eigenstates $F_{ss'}(\mathbf{k}, \mathbf{k}')$ is given by

$$F_{ss'}(\mathbf{k}, \mathbf{k}') = \frac{1 + ss' \cos \theta_{\mathbf{k}\mathbf{k}'}}{2}, \quad (8)$$

where $\theta_{\mathbf{k}\mathbf{k}'}$ is the angle between the 3D wave vectors \mathbf{k}' and \mathbf{k} with $\mathbf{k}' = \mathbf{k} + \mathbf{q}$. $f(x) = [1 + \exp\{\beta(x - \mu)\}]^{-1}$ is the Fermi distribution function with $\beta = 1/k_B T$.

To proceed with the theoretical details, we assume zero temperature $T = 0$ K. The Fermi distribution function $f(x)$ turns into a simple step function $\theta(\mu - x)$. Because of the general relation of the polarization function $\Pi(q, -\omega) = [\Pi(q, \omega)]^*$, we can restrict our discussion to the positive frequency case $\omega > 0$. In the rest of the calculation, we will set $\hbar = v_F = 1$, which immediately implies the relation of $\mu = k_F$.

III. UNDOPED WEYL SEMIMETALS

In general, for a system with particle-hole symmetry, its polarization function depends only on the magnitude of chemical potential (see Appendix B), namely, $\Pi(q, \omega, \mu) = \Pi(q, \omega, -\mu) = \Pi(q, \omega, |\mu|)$. Therefore, we come to a conclusion that the polarization function of undoped Weyl SMs with the chirality-dependent chemical potentials μ_\pm is identical to that of doped Weyl SMs with chemical potential $\mu = |\mu_\pm|$.

Next we set out to find the plasmon dispersion, which can be obtained within the RPA by finding zeros of the dielectric function,

$$\varepsilon(q, \omega - i\Gamma) = 0, \quad (9)$$

where Γ is the decay rate of the plasmon. For weak damping, Eq. (9) reduces to the following approximate equation

$$\text{Re } \varepsilon(q, \omega) = 0. \quad (10)$$

For the long wavelength approximation $q \ll \omega \ll \mu$, due to $\text{Im } \varepsilon(q \rightarrow 0, \omega) = 0$, Eq. (9) reduces to

$$\text{Re } \varepsilon(q \rightarrow 0, \omega) = 0. \quad (11)$$

To order q^0 , the real part of the dielectric function has the form

$$\text{Re } \varepsilon(q \rightarrow 0, \omega) = \kappa^*(\omega) - \frac{4\alpha_\kappa g \mu^2}{3\pi\omega^2}, \quad (12)$$

where the function $\kappa^*(\omega)$ is defined as

$$\kappa^*(\omega) = 1 + \frac{\alpha_\kappa g}{3\pi} \log \left| \frac{4\Lambda^2}{4\mu^2 - \omega^2} \right| \quad (13)$$

with $\alpha_\kappa = e^2/\kappa$ the effective fine structure constant. Substituting Eq. (12) into Eq. (11) yields

$$\omega_0 = \sqrt{\frac{\alpha_\kappa}{\kappa^*(\omega_0)}} \sqrt{\frac{4g\mu^2}{3\pi}}. \quad (14)$$

Neglecting the logarithmic corrections in Eq. (13), we can obtain the lowest plasmon frequency $\omega_0 \approx \sqrt{\frac{4g\alpha_\kappa\mu^2}{3\pi}}$. Two remarks are in order here. First, the linear dependence of ω_0 on μ also holds for the Dirac SMs³⁶ and Weyl SMs in the absence of the chiral anomaly³⁸. Second, recalling the chirality-dependent chemical potential in Eq. (4), one immediately finds that $\omega_0 \propto |\mathbf{B}|^{1/3}$. Note that this result is different from previous work in the limit of a strong magnetic field^{12,39}. In Ref. 12 the plasmon frequency is found to be proportional to $|\mathbf{B}|^{1/2}$ in the intrinsic case, whereas Ref. 39 only considered the doped case.

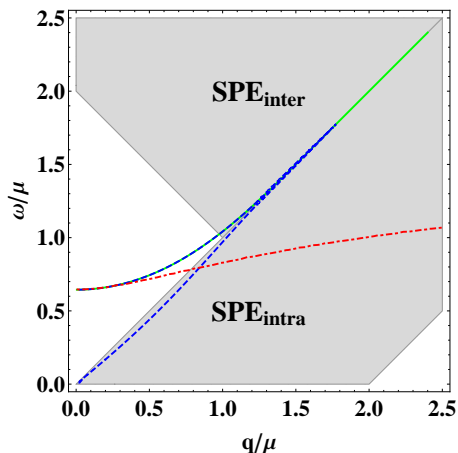


FIG. 2: (Color online) Plasmon modes in undoped 3D Weyl SMs with chiral anomaly, i.e., $\mathbf{E} \cdot \mathbf{B} \neq 0$ are calculated within the RPA. The red dotted-dashed line shows the long wavelength plasmon mode, the blue dashed line corresponds to the approximate solution obtained from Eq. (10), and the green solid line represents the exact solution of Eq. (9). The shaded area indicates the intraband and interband SPE regions⁴⁰.

Taking into account the leading order contribution of q , we get

$$\begin{aligned} \text{Re } \varepsilon(q \rightarrow 0, \omega) & \\ = \kappa^*(\omega) - \frac{4\alpha_\kappa g \mu^2}{3\pi\omega^2} \left[1 - \frac{q^2}{(2\mu)^2} (1 + \mathcal{F}(2\mu, \omega)) \right], & \quad (15) \end{aligned}$$

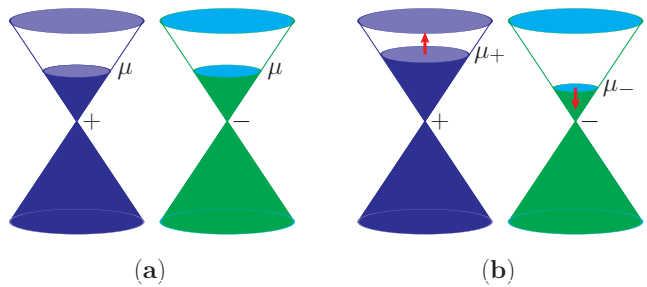


FIG. 3: (Color online) (a) is the equilibrium distribution of electrons in the two Weyl nodes without chiral anomaly ($\mathbf{E} \cdot \mathbf{B} = 0$). (b) is the Fermi levels of the Weyl nodes shift away from the equilibrium position μ due to the chiral anomaly ($\mathbf{E} \cdot \mathbf{B} \neq 0$). μ_\pm are the resulting chirality-dependent chemical potentials.

with $\mathcal{F}(x, y) = \frac{x^4(y^2 - \frac{3}{5}x^2)}{y^2(x^2 - y^2)^2}$. To gain some insight into the long wavelength plasmon dispersion, we write down an approximate expression from Eqs. (11) and (15) as

$$\omega \approx \omega_0 \left[1 - \frac{q^2}{8\mu^2} (1 + \mathcal{F}(2\mu, \omega_0)) \right]. \quad (16)$$

For comparison, we compute the exact solution, the long wavelength solution, and the approximate solution, respectively, which are plotted in Fig. 2. In the long wavelength regime, all the three solutions are in good agreement with each other⁴⁰. The neglect of the logarithmic term in Eq. (13) that underlies measurable consequences⁴¹ would enhance the plasmon frequency. It should be noted that the lower branch of the approximate solution is fully in the intraband single particle excitation (SPE) region, which is merely an artifact due to the weak damping approximation of Eq. (9).

IV. DOPED WEYL SEMIMETALS

Now we turn to investigate the effect of the chiral anomaly on the plasmon mode in doped Weyl SMs. Simultaneously turning on the parallel electric field \mathbf{E} and magnetic field \mathbf{B} , the amount of electrons transferred from one Weyl node to the other is equal to $\Delta\rho_\chi$, with the result that the Fermi surface of one Weyl node shifts upward and the other shifts downward (see Fig. 3). We assign the chirality-dependent chemical potential μ_\pm for the large and small Fermi surfaces with $\mu_+ > |\mu_-|$. In the long wavelength approximation $q \ll \omega \ll |\mu_-| \leq \mu_+$, to order q^2 , the real part of the polarization function takes the form

$$\begin{aligned} \text{Re } \varepsilon(q \rightarrow 0, \omega) &= \kappa^*(\omega) - \frac{2\alpha_\kappa g (\mu_+^2 + \mu_-^2)}{3\pi\omega^2} \\ &\times \left[1 - \frac{q^2}{4(\mu_+^2 + \mu_-^2)} \sum_{\lambda=\pm} (1 + \mathcal{F}(2\mu_\lambda, \omega_0)) \right]. \quad (17) \end{aligned}$$

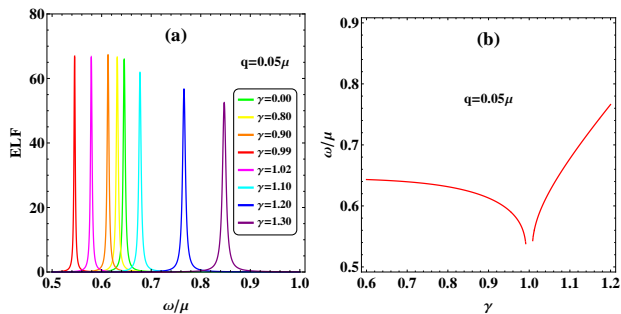


FIG. 4: (Color online) (a) shows the energy loss function for a series of values of γ in doped Weyl SMs with the chiral anomaly. (b) is the dependence of frequencies of the undamped plasmon mode on the ratio γ . The LT occurs at the turning point of the plasmon dispersion⁴⁰.

To obtain an approximate behavior of the long wavelength plasmon dispersion, one can arrive at an expression from Eqs. (11) and (17) as

$$\omega \approx \omega_0 \left[1 - \frac{q^2}{8(\mu_+^2 + \mu_-^2)} \sum_{\lambda=\pm} (1 + \mathcal{F}(2\mu_\lambda, \omega_0)) \right]. \quad (18)$$

where the notations $\kappa^*(\omega)$ and ω_0 are given by

$$\omega_0 = \sqrt{\frac{\alpha_\kappa}{\kappa^*(\omega_0)}} \sqrt{\frac{2g}{3\pi}(\mu_+^2 + \mu_-^2)}, \quad (19)$$

$$\kappa^*(\omega) = 1 + \frac{\alpha_\kappa g}{6\pi} \left(\sum_{\lambda=\pm} \log \left| \frac{4\Lambda^2}{4\mu_\lambda^2 - \omega^2} \right| \right), \quad (20)$$

which can be traced back to the counterpart of Eq. (14) in the undoped case by taking $\mu_+ = \mu_-$.

The plasmons can also be revealed as sharp peaks in the energy loss function (ELF), defined as the imaginary part of the inverse dielectric function, i.e., $\text{Im}[1/\varepsilon(q, \omega)]$ that can be probed in various spectroscopy experiments, such as the electron energy-loss spectroscopy. As shown in Fig. 4(a), in the presence of the chiral anomaly the plasmon exhibits some exotic features in the ELF spectrum. As long as the ratio γ gradually increases from 0 to 1, the plasmon frequency with chiral anomaly ω_{ch} has a redshift with respect to the frequency without chiral anomaly ω_{eq} and finally reaches a minimum ω_{min} . On the other hand, once the small Fermi surface crosses the Weyl node, i.e., $\gamma > 1$, the plasmon frequency becomes larger than ω_{min} and then has a continuous violetshift. The behavior of plasmons of doped Weyl SMs under the influence of the chiral anomaly can be captured by our long wavelength expressions in Eq. (19) and summarized

as follows

$$\begin{cases} \omega_{\text{min}} < \omega_{\text{ch}} < \omega_{\text{eq}}, & 0 < \gamma < 1; \\ \omega_{\text{min}} < \omega_{\text{ch}}, & 1 < \gamma. \end{cases} \quad (21)$$

Therefore, the unique features of undamped plasmon mode can clearly characterize the chiral anomaly in doped Weyl SMs. It should be emphasized that compared with other methods^{31–34}, our method possesses the advantage that we can directly determine the position of the chirality-dependent LT point from the plasmon dispersion, as shown in Fig. 4(b), which coincides with the minimal frequency of plasmon mode. Actually, when $|\gamma - 1| \rightarrow 0$, the small Fermi level is close to the Weyl node point, such that small energy or momentum could induce interband transition and lead to a large number of electron-hole excitations. The plasmon mode will be damped by these electron-hole excitations. Increasing q will broaden the damping region (see Fig. 4(b)). Hence, the fate of the plasmon mode indeed connects with the chirality-dependent LT.

V. CONCLUSIONS

In summary, we investigated the chiral anomaly effect on the plasmon mode in 3D Weyl SMs within the RPA. We proved that a new plasmon mode would emerge in undoped Weyl SMs due to the chiral anomaly. We also demonstrated the unusual properties of the plasmon mode in doped Weyl SMs and further pointed out that the plasmon can be taken as a fingerprint of the chiral anomaly. Finally, we showed how to identify the chirality-dependent LT point from the plasmon dispersion. Our work sheds light on the probing of the chiral anomaly in 3D Weyl SMs via the plasmon mode. The tunability of plasmons due to the chiral anomaly also makes Weyl SMs promising candidates for plasmonics⁴².

ACKNOWLEDGMENTS

We are grateful to Yuanpei Lan, Min Lv, Wen-Yu Shan and Hui Zhang for stimulating discussions, to Ran Cheng, Matthew Daniels and Furu Zhang for a careful reading of the manuscript. This work is supported by NSF EFRI (No. 1433496), the Scientific Research Fund of the Education Department of Sichuan Province under Grant No. 13ZB0157, the NSFC under Grants Nos. 11074234, 11274286.

Appendix A: The calculation of the polarization function with positive chemical potential

In this appendix we present the major steps of calculating the polarization function of a Weyl node with positive chemical potential $+\mu$ in the 3D Weyl semimetal. Those of the other Weyl nodes can be obtained in a similar manner. The polarization function can be decomposed into two parts

$$\Pi(q, \omega) = \Pi^-(q, \omega) + \Pi^+(q, \omega), \quad (\text{A1})$$

where $\Pi^\pm(q, \omega)$ are defined by

$$\Pi^-(q, \omega) = \frac{g}{L^3} \sum_{\mathbf{k}} \left(\frac{[f(\epsilon_{\mathbf{k}-}) - f(\epsilon_{\mathbf{k}'-})](1 + \cos \theta_{\mathbf{k}\mathbf{k}'})/2}{\hbar\omega + \epsilon_{\mathbf{k}-} - \epsilon_{\mathbf{k}'-} + i\eta} + \frac{f(\epsilon_{\mathbf{k}-})(1 - \cos \theta_{\mathbf{k}\mathbf{k}'})/2}{\hbar\omega + \epsilon_{\mathbf{k}-} - \epsilon_{\mathbf{k}'+} + i\eta} - \frac{f(\epsilon_{\mathbf{k}'-})(1 - \cos \theta_{\mathbf{k}\mathbf{k}'})/2}{\hbar\omega + \epsilon_{\mathbf{k}-} - \epsilon_{\mathbf{k}'-} + i\eta} \right), \quad (\text{A2})$$

$$\Pi^+(q, \omega) = \frac{g}{L^3} \sum_{\mathbf{k}} \left(\frac{[f(\epsilon_{\mathbf{k}+}) - f(\epsilon_{\mathbf{k}'+})](1 + \cos \theta_{\mathbf{k}\mathbf{k}'})/2}{\hbar\omega + \epsilon_{\mathbf{k}+} - \epsilon_{\mathbf{k}'+} + i\eta} + \frac{f(\epsilon_{\mathbf{k}+})(1 - \cos \theta_{\mathbf{k}\mathbf{k}'})/2}{\hbar\omega + \epsilon_{\mathbf{k}+} - \epsilon_{\mathbf{k}'-} + i\eta} - \frac{f(\epsilon_{\mathbf{k}'+})(1 - \cos \theta_{\mathbf{k}\mathbf{k}'})/2}{\hbar\omega + \epsilon_{\mathbf{k}-} - \epsilon_{\mathbf{k}'+} + i\eta} \right). \quad (\text{A3})$$

Due to the causality $\text{Re } \Pi^-(q, -\omega) = \text{Re } \Pi^-(q, \omega)$, in the following we focus only on the case for $\omega > 0$. We firstly evaluate the polarization function of the intrinsic case with $\mu = 0$ that implies $\Pi^+(q, \omega)$ vanishes. After some simple algebra, we can obtain

$$\Pi^-(q, \omega) = -\frac{g}{16\pi^2 q} \int_0^\Lambda dk \int_{|k-q|}^{k+q} dk' [(k' - k)^2 - q^2] \left(\frac{1}{\omega - k - k' + i\eta} - \frac{1}{\omega + k + k' + i\eta} \right), \quad (\text{A4})$$

where Λ is the cutoff. Using the Dirac identity $\frac{1}{x \pm i\eta} = \mathcal{P} \frac{1}{x} \mp i\pi \delta(x)$ one can get

$$\text{Im } \Pi^-(q, \omega) = \frac{g}{16\pi q} \int_0^\Lambda dk \int_{|k-q|}^{k+q} dk' [(k' - k)^2 - q^2] \delta(\omega - k - k'), \quad (\text{A5})$$

$$\text{Re } \Pi^-(q, \omega) = -\frac{g}{16\pi^2 q} \mathcal{P} \int_0^\Lambda dk \int_{|k-q|}^{k+q} dk' [(k' - k)^2 - q^2] \left(\frac{1}{\omega - k - k'} - \frac{1}{\omega + k + k'} \right), \quad (\text{A6})$$

where the notation \mathcal{P} means the principal value of the integral. It is straightforward to calculate the imaginary part of the intrinsic polarization function

$$\text{Im } \Pi^-(q, \omega) = -\frac{gq^2 \theta(\omega - q)}{24\pi}. \quad (\text{A7})$$

In fact, there are two different methods to calculate the real part of the polarization function. One is to directly carry out the integral. The other is to apply the Kramers-Krönig relation.

We at first perform the integration Eq.(A6) to get the real part of the intrinsic polarization function. It is convenient to decompose this real part into two terms

$$\text{Re } \Pi^-(q, \omega) = \text{Re } \Pi_1^-(q, \omega) + \text{Re } \Pi_2^-(q, \omega), \quad (\text{A8})$$

where

$$\text{Re } \Pi_1^-(q, \omega) = \frac{g}{16\pi^2 q} \mathcal{P} \int_0^\Lambda dk \int_{|k-q|}^{k+q} dk' \left((-3k + k') + \frac{(2k + \omega)^2 - q^2}{k' + k + \omega} \right), \quad (\text{A9})$$

$$\text{Re } \Pi_2^-(q, \omega) = \frac{g}{16\pi^2 q} \mathcal{P} \int_0^\Lambda dk \int_{|k-q|}^{k+q} dk' \left((-3k + k') + \frac{(2k - \omega)^2 - q^2}{k' + k - \omega} \right). \quad (\text{A10})$$

After some cumbersome but straightforward calculation, we can get

$$\begin{aligned} \text{Re } \Pi_1^-(q, \omega) &= -\frac{2gq^2}{96\pi^2} \log \frac{(2\Lambda + \omega)^2 - q^2}{(q + \omega)^2} + \frac{g}{96\pi^2} [+6\omega(q + 2\Lambda)] \\ &+ \frac{g}{96\pi^2} \left[\frac{(2\Lambda + \omega)^3}{q} \log \frac{2\Lambda + \omega + q}{2\Lambda + \omega - q} - 2(2\Lambda + \omega)^2 - 3q(2\Lambda + \omega) \log \frac{2\Lambda + \omega + q}{2\Lambda + \omega - q} + \frac{16}{3}q^2 \right], \end{aligned} \quad (\text{A11})$$

$$\begin{aligned} \text{Re } \Pi_2^-(q, \omega) &= -\frac{2gq^2}{96\pi^2} \log \frac{(2\Lambda - \omega)^2 - q^2}{(q - \omega)^2} + \frac{g}{96\pi^2} [-6\omega(q + 2\Lambda)] \\ &+ \frac{g}{96\pi^2} \left[\frac{(2\Lambda - \omega)^3}{q} \log \frac{2\Lambda - \omega + q}{2\Lambda - \omega - q} - 2(2\Lambda - \omega)^2 - 3q(2\Lambda - \omega) \log \frac{2\Lambda - \omega + q}{2\Lambda - \omega - q} + \frac{16}{3}q^2 \right]. \end{aligned} \quad (\text{A12})$$

and

$$\begin{aligned} \text{Re } \Pi^-(q, \omega) = & -\frac{2gq^2}{96\pi^2} \left(\log \frac{(2\Lambda + \omega)^2 - q^2}{(q + \omega)^2} + \log \frac{(2\Lambda - \omega)^2 - q^2}{(q - \omega)^2} \right) \\ & + \frac{g}{96\pi^2} \left[\frac{(2\Lambda + \omega)^3}{q} \log \frac{2\Lambda + \omega + q}{2\Lambda + \omega - q} - 2(2\Lambda + \omega)^2 - 3q(2\Lambda + \omega) \log \frac{2\Lambda + \omega + q}{2\Lambda + \omega - q} + \frac{16}{3}q^2 \right] \\ & + \frac{g}{96\pi^2} \left[\frac{(2\Lambda - \omega)^3}{q} \log \frac{2\Lambda - \omega + q}{2\Lambda - \omega - q} - 2(2\Lambda - \omega)^2 - 3q(2\Lambda - \omega) \log \frac{2\Lambda - \omega + q}{2\Lambda - \omega - q} + \frac{16}{3}q^2 \right]. \end{aligned} \quad (\text{A13})$$

Two remarks about the real part of the intrinsic polarization function are in order here. First, $\text{Re } \Pi_2^-(q, \omega)$ can also be obtained by replacing ω with $-\omega$ in $\text{Re } \Pi_1^-(q, \omega)$. Second, it can be seen that $\text{Re } \Pi^-(q, \omega)$ is an even function in ω and will be valid for an arbitrary frequency.

Since the cutoff Λ is much larger than both q and ω , it is instructive to take a look at the expression of $\text{Re } \Pi^-(q, \omega)$ in large Λ limit. Making use of the limits

$$\lim_{\frac{t}{q} \rightarrow \infty} \left(\frac{t^3}{q} \log \frac{t+q}{t-q} - 2t^2 \right) = \frac{2q^2}{3}, \quad \lim_{\frac{t}{q} \rightarrow \infty} t \log \frac{t+q}{t-q} = 2q, \quad (\text{A14})$$

we immediately verify that these underlined terms in Eq.(A13) vanish with $t = 2\Lambda \pm \omega$ and then get a simple expression of $\text{Re } \Pi^-(q, \omega)$

$$\text{Re } \Pi^-(q, \omega) = -\frac{gq^2}{48\pi^2} \log \left(\frac{(2\Lambda + \omega)^2 - q^2}{(q + \omega)^2} \frac{(2\Lambda - \omega)^2 - q^2}{(q - \omega)^2} \right). \quad (\text{A15})$$

We can further simplify the terms of q and ω in the numerator of the logarithmic function and have

$$\text{Re } \Pi^-(q, \omega) = -\frac{gq^2}{24\pi^2} \log \left| \frac{4\Lambda^2}{q^2 - \omega^2} \right|. \quad (\text{A16})$$

Now we turn to calculate the real part of the intrinsic polarization function $\Pi^-(q, \omega)$ using the Kramers-Krönig relations. Since the imaginary part does not approach zero as $\omega \rightarrow \infty$ one need to utilize the generalized Kramers-Krönig relation with one subtraction³⁷,

$$\text{Re } \Pi^-(q, \omega) = \text{Re } \Pi^-(q, 0) + \frac{\omega}{\pi} \mathcal{P} \int_{-\infty}^{\infty} d\xi \frac{\text{Im } \Pi^-(q, \xi)}{\xi(\xi - \omega)}, \quad (\text{A17})$$

$$\text{Im } \Pi^-(q, \omega) = \text{Im } \Pi^-(q, 0) - \frac{\omega}{\pi} \mathcal{P} \int_{-\infty}^{\infty} d\xi \frac{\text{Re } \Pi^-(q, \xi)}{\xi(\xi - \omega)}. \quad (\text{A18})$$

The zero frequency term $\text{Re } \Pi^-(q, 0)$ in Eq.(A17) can be obtained from Eq. (A6)

$$\text{Re } \Pi^-(q, 0) = -\frac{4gq^2}{96\pi^2} \log \frac{(2\Lambda)^2 - q^2}{q^2} + \frac{2g}{96\pi^2} \left[\frac{(2\Lambda)^3}{q} \log \frac{2\Lambda + q}{2\Lambda - q} - 2(2\Lambda)^2 - 3q(2\Lambda) \log \frac{2\Lambda + q}{2\Lambda - q} + \frac{16}{3}q^2 \right]. \quad (\text{A19})$$

In the limit of large cutoff Λ , we find that the above underlined term vanishes. Neglecting the q^2 term in the numerator of the logarithmic function yields

$$\text{Re } \Pi^-(q, 0) = -\frac{gq^2}{24\pi^2} \log \frac{4\Lambda^2}{q^2}. \quad (\text{A20})$$

The second term in Eq.(A17) is calculated by carrying out the integration

$$\text{Re } \Pi^-(q, \omega) - \text{Re } \Pi^-(q, 0) = \frac{\omega}{\pi} \mathcal{P} \int_{-\infty}^{\infty} d\xi \frac{\text{Im } \Pi^-(q, \xi)}{\xi(\xi - \omega)} = -\frac{gq^2}{24\pi^2} \log \left| \frac{q^2}{q^2 - \omega^2} \right|. \quad (\text{A21})$$

Substituting Eq.(A20) into Eq.(A21) leads to the same result as Eq.(A16), which differs slightly from the counterpart in Ref³⁸. It should be pointed out that $\text{Re } \Pi^-(q, \omega)$ satisfies Eq.(A18) by considering $\text{Im } \Pi^-(q, 0) = 0$. Therefore, the polarization function of the intrinsic case turns out to be

$$\Pi^-(q, \omega) = -\frac{gq^2}{24\pi^2} \left[\log \left| \frac{4\Lambda^2}{q^2 - \omega^2} \right| + i\pi\theta(\omega - q) \right]. \quad (\text{A22})$$

Following the similar procedure, one can reach the polarization function $\Pi^+(q, \omega)$ of the extrinsic case with $\mu > 0$

$$\begin{aligned} \text{Im } \Pi^+(q, \omega) = & -\frac{gq^2}{8\pi^2} \left[\theta(q - \omega) \left(\frac{\pi G(q, \omega)}{q^2} \theta(2\mu + \omega - q) - \frac{\pi G(q, -\omega)}{q^2} \theta(2\mu - \omega - q) \right) \right. \\ & \left. + \theta(\omega - q) \left(-\frac{\pi}{3} \theta(2\mu - \omega - q) - \frac{\pi G(-q, -\omega)}{q^2} \theta(q + \omega - 2\mu) \theta(2\mu + q - \omega) \right) \right], \end{aligned} \quad (\text{A23})$$

$$\begin{aligned} \text{Re } \Pi^+(q, \omega) = & -\frac{gq^2}{8\pi^2} \left[\frac{8\mu^2}{3q^2} - \frac{G(q, \omega)H(q, \omega)}{q^2} - \frac{G(-q, \omega)H(-q, \omega)}{q^2} - \frac{G(q, -\omega)H(q, -\omega)}{q^2} \right. \\ & \left. - \frac{G(-q, -\omega)H(-q, -\omega)}{q^2} \right], \end{aligned} \quad (\text{A24})$$

where the functions $G(q, \omega)$ and $H(q, \omega)$ are defined by

$$G(q, \omega) = \frac{1}{12q} [(2\mu + \omega)^3 - 3q^2(2\mu + \omega) + 2q^3], \quad (\text{A25})$$

$$H(q, \omega) = \log \left| \frac{2\mu + \omega - q}{q - \omega} \right|. \quad (\text{A26})$$

Combining $\Pi^-(q, \omega)$ with $\Pi^+(q, \omega)$, we finally obtain the total polarization function for a Weyl node with positive chemical potential $+\mu$ in the 3D Weyl semimetal in Eq.(A1).

Appendix B: The equivalence of the polarization functions with opposite chemical potentials

In this appendix we will prove the equivalence of the polarization functions with opposite chemical potentials for a system with particle-hole symmetry. The polarization function for the other node with negative chemical potential $-\mu$ can be written as

$$\tilde{\Pi}(q, \omega) = \frac{g}{L^3} \sum_{\mathbf{k}ss'} \frac{\tilde{f}(\tilde{\epsilon}_{\mathbf{k}s}) - \tilde{f}(\tilde{\epsilon}_{\mathbf{k}'s'})}{\hbar\omega + \tilde{\epsilon}_{\mathbf{k}s} - \tilde{\epsilon}_{\mathbf{k}'s'} + i\eta} F_{ss'}(\mathbf{k}, \mathbf{k}'), \quad (\text{B1})$$

where the function $\tilde{f}(x)$ is defined as $\tilde{f}(x) = [1 + \exp\{\beta(x + \mu)\}]^{-1}$. The particle-hole symmetry of Weyl nodes enables us to relabel the energy dispersions in the following way: $\tilde{\epsilon}_{\mathbf{k}s} \rightarrow -\epsilon_{\mathbf{k}s}$ and write

$$\tilde{\Pi}(q, \omega) = \frac{g}{L^3} \sum_{\mathbf{k}ss'} \frac{\tilde{f}(-\epsilon_{\mathbf{k}s}) - \tilde{f}(-\epsilon_{\mathbf{k}'s'})}{\hbar\omega - \epsilon_{\mathbf{k}s} + \epsilon_{\mathbf{k}'s'} + i\eta} F_{ss'}(\mathbf{k}, \mathbf{k}'). \quad (\text{B2})$$

Utilizing the property of the Fermi distribution function $f(x) + \tilde{f}(-x) = 1$ leads to

$$\tilde{\Pi}(q, \omega) = \frac{g}{L^3} \sum_{\mathbf{k}ss'} \frac{f(\epsilon_{\mathbf{k}'s'}) - f(\epsilon_{\mathbf{k}s})}{\hbar\omega + \epsilon_{\mathbf{k}'s'} - \epsilon_{\mathbf{k}s} + i\eta} F_{ss'}(\mathbf{k}, \mathbf{k}'). \quad (\text{B3})$$

One can immediately observe the relation

$$[\tilde{\Pi}(q, -\omega)]^* = \frac{g}{L^3} \sum_{\mathbf{k}ss'} \frac{f(\epsilon_{\mathbf{k}s}) - f(\epsilon_{\mathbf{k}'s'})}{\hbar\omega + \epsilon_{\mathbf{k}s} - \epsilon_{\mathbf{k}'s'} + i\eta} F_{ss'}(\mathbf{k}, \mathbf{k}'). \quad (\text{B4})$$

It is obvious that $[\tilde{\Pi}(q, -\omega)]^*$ is nothing but the definition of the polarization function with a positive chemical potential μ . Recalling the general property of $\Pi(q, -\omega) = [\Pi(q, \omega)]^*$, we arrive at the desirable result

$$\Pi(q, \omega) = \tilde{\Pi}(q, \omega). \quad (\text{B5})$$

* Electronic address: jhzhou@andrew.cmu.edu

† Electronic address: hrchang@mail.ustc.edu.cn

- ¹ G. E. Volovik, *The Universe in a Helium Droplet* (Clarendon Press, Oxford, 2003).
- ² H. B. Nielsen and M. Ninomiya, Phys. Lett. B **130**, 389 (1983).
- ³ Di Xiao, Ming-Che Chang, and Qian Niu, Rev. Mod. Phys. **82**, 1959 (2010).
- ⁴ K. Y. Yang, Y. M. Lu, and Y. Ran, Phys. Rev. B **84**, 075129, (2011).
- ⁵ P. Hosur, S. A. Parameswaran, and A. Vishwanath, Phys. Rev. Lett. **108**, 046602 (2012).
- ⁶ V. Aji, Phys. Rev. B **85**, 241101 (2012).
- ⁷ A. A. Zyuzin and A. A. Burkov, Phys. Rev. B. **86**, 115133 (2012).
- ⁸ Adolfo G. Grushin, Phys. Rev. D **86**, 045001 (2012).
- ⁹ J. H. Zhou, H. Jiang, Q. Niu, and J. R. Shi, Chinese Phys. Lett. **30**, 027101 (2013).
- ¹⁰ P. E. C. Ashby and J. P. Carbotte, Phys. Rev. B **87**, 245131 (2013).
- ¹¹ M. M. Vazifeh and M. Franz, Phys. Rev. Lett. **111**, 027201 (2013).
- ¹² D. T. Son and B. Z. Spivak, Phys. Rev. B **88**, 104412 (2013).
- ¹³ P. Goswami, S. Tewari, Phys. Rev. B **88**, 245107 (2013).
- ¹⁴ K. Landsteiner, Phys. Rev. B **89**, 075124 (2014).
- ¹⁵ G. Basar, D. E. Kharzeev, and Ho-Ung Yee, Phys. Rev. B **89**, 035142 (2014).
- ¹⁶ S. T. Ramamurthy and T. L. Hughes, arXiv:1405.7377.
- ¹⁷ X. G. Wan, A. M. Turner, A. Vishwanath, and Sergey Y. Savrasov, Phys. Rev. B. **83**, 205101 (2011).
- ¹⁸ A. A. Burkov and L. Balents, Phys. Rev. Lett. **107**, 127205 (2011).
- ¹⁹ G. B. Halász and L. Balents, Phys. Rev. B **85**, 035103 (2012).
- ²⁰ G. Xu, H. M. Weng, Z. J. Wang, X. Dai, and Z. Fang, Phys. Rev. Lett. **107**, 186806 (2011).
- ²¹ A. A. Zyuzin, Si Wu, and A. A. Burkov, Phys. Rev. B **85**, 165110 (2012).
- ²² W. Witczak-Krempa and Y. B. Kim, Phys. Rev. B **85**, 045124 (2012).
- ²³ J. L. Mañes, Phys. Rev. B **85**, 155118 (2012).
- ²⁴ S. Borisenko, Q. Gibson, D. Evtushinsky, V. Zabolotnyy, B. Buechner and R. J. Cava, Phys. Rev. Lett. **113**, 027603 (2014).
- ²⁵ Zhijun Wang, Hongming Weng, Quansheng Wu, Xi Dai, and Zhong Fang, Phys. Rev. B **88**, 125427 (2013).
- ²⁶ Z. K. Liu, B. Zhou, Y. Zhang, Z. J. Wang, H. M. Weng, D. Prabhakaran, S.-K. Mo, Z. X. Shen, Z. Fang, X. Dai, Z. Hussain and Y. L. Chen, Science **343**, 864 (2014).
- ²⁷ Zhijun Wang, Yan Sun, Xing-Qiu Chen, Cesare Franchini, Gang Xu, Hongming Weng, Xi Dai, and Zhong Fang, Phys. Rev. B **85**, 195320 (2012).
- ²⁸ S. Adler, Phys. Rev. **177**, 2426 (1969).
- ²⁹ J. S. Bell and R. Jackiw, Nuovo Cimento 60A, 4 (1969).
- ³⁰ H. J. Kim, K. S. Kim, J.-F. Wang, M. Sasaki, N. Satoh, A. Ohnishi, M. Kitaura, M. Yang, and L. Li, Phys. Rev. Lett. **111**, 246603 (2013).
- ³¹ S. A. Parameswaran, T. Grover, D. A. Abanin, D. A. Pesin, and A. Vishwanath, arXiv:1306.1234.
- ³² P. Hosur, Xiao-Liang Qi, arXiv:1401.2762.
- ³³ P. Goswami, G. Sharma, and S. Tewari, arXiv:1404.2927.
- ³⁴ P. E. C. Ashby, J. P. Carbotte, arXiv:1405.7034.
- ³⁵ In general, when the energy difference between the zeroth and the first Landau Levels (LLs) $E_L = \hbar\omega_c$ (ω_c is the cyclotron frequency) is smaller than the thermal excitation energy $E_T = k_B T$ or the inverse scattering time, these broaden effects could smear the LLs. As a result, we can neglect the LL quantization.
- ³⁶ S. Das Sarma and E. H. Hwang, Phys. Rev. Lett. **102**, 206412 (2009).
- ³⁷ J. D. Bjorken and S. D. Drell, *Relativistic Quantum Fields*, (McGraw-Hill, New York, 1965).
- ³⁸ M. Lv and S. C. Zhang, Int. J. Mod. Phys. B **27**, 1350177 (2013).
- ³⁹ I. Panfilov, A. A. Burkov and D. A. Pesin, Phys. Rev. B **89**, 245103 (2014).
- ⁴⁰ In our numerical calculation, we make use of the parameters: $g = 12$ (for the materials predicted in Ref¹⁷) and the cutoff of wave vector $\Lambda = 10\mu$, Fermi velocity $v_F = 6.85 \times 10^5 \text{ m} \cdot \text{s}^{-1}$, effective dielectric constant $\kappa = 20$. It should be noted that the different values of these parameters just quantitatively change the plasmon frequency. For the typical parameters³⁴ of $|\mathbf{B}|=1$ Tesla, $|\mathbf{E}| = 10^3$ V/m and $\tau_v = 10$ ps, we estimate the plasmon frequency in the long-wave regime roughly in the order of meV.
- ⁴¹ Bitan Roy and Jay D. Sau, arXiv:1406.4501.
- ⁴² S. A. Maier, *Plasmonics: Fundamentals and Applications* (Springer, 2007).